Monthly Notices
of the
ROYAL ASTRONOMICAL SOCIETY

Mon. Not. R. Astron. Soc. **400,** 589–602 (2009) doi:10.1111/j.1365-2966.2009.15491.x

The ionization of the emission-line gas in young radio galaxies

J. Holt,[1⋆] C. N. Tadhunter[2] and R. Morganti[3,4]

[1]*Leiden Observatory, Leiden University, PO Box 9513, 2300 RA Leiden, the Netherlands*
[2]*Department of Physics and Astronomy, University of Sheffield, Sheffield S3 7RH*
[3]*Netherlands Institute for Radio Astronomy, Postbus 2, 7990 AA Dwingeloo, the Netherlands*
[4]*Kapteyn Astronomical Institute, University of Groningen, Postbus 800, 9700 AV Groningen, the Netherlands*

Accepted 2009 August 3. Received 2009 July 29; in original form 2009 May 13

ABSTRACT

This paper is the second in a series in which we present intermediate-resolution, wide-wavelength coverage spectra for a complete sample of 14 compact radio sources, taken with the aim of investigating the impact of the nuclear activity on the circumnuclear interstellar medium (ISM) in the early stages of radio source evolution. In the first paper (Holt, Tadhunter & Morganti), we presented the kinematic results from the nuclear emission-line modelling and reported fast outflows in the circumnuclear gas. In this paper, we use the line fluxes to investigate the physical conditions and dominant ionization mechanisms of the emission-line gas. We find evidence for large electron densities and high reddening in the nuclear regions, particularly in the broader, blueshifted components. These results are consistent with the idea that the young, recently triggered radio sources still reside in dense and dusty cocoons deposited by the recent activity triggering event (merger/interaction). In addition, we find that the quiescent nuclear and extended narrow components are consistent with active galactic nucleus (AGN) photoionization, split between simple-slab AGN photoionization and mixed-medium photoionization models. For the nuclear broader and shifted components, the results are less clear. Whilst there are suggestions that the broader components may be closer to shock plus precursor models on the diagnostic diagrams, and that the electron temperatures and densities are high, we are unable to unambiguously distinguish the dominant ionization mechanism using the optical emission-line ratios. This is surprising given the strong evidence for jet–cloud interactions (broad emission lines, large outflow velocities and strong radio-optical alignments), which favours the idea that the warm gas has been accelerated in shocks driven by the radio lobes expanding through a dense cocoon of gas deposited during the triggering event.

Key words: ISM: jets and outflows – galaxies: active – galaxies: ISM – galaxies: kinematics and dynamics.

1 INTRODUCTION

It is now understood that the active galactic nucleus (AGN) feedback, in the form of outflows in the circumnuclear interstellar medium (ISM), is likely to be a crucial part of galaxy evolution and is responsible for the close relationship between the black hole mass and the galaxy bulge properties (e.g. Ferrarese & Merritt 2000; Gebhardt et al. 2000; Tremaine et al. 2002; Marconi & Hunt 2003). However, due to a lack of observational evidence, feedback is often invoked as a 'black box' and often relies on powerful AGN winds to drive the outflows and shed the natal cocoon deposited during the triggering event (e.g. merger/interaction; Di Matteo, Springel & Hernquist 2005; Hopkins et al. 2005). Whilst this may be true for radio-quiet AGN, it is likely that in radio-loud AGN, the expanding radio jets also contribute to the feedback through jet-induced outflows (e.g. Bicknell, Dopita & O'Dea 1997), particularly during the early stages of the radio source evolution when the radio source and ISM are on similar scales.

Recent work (by e.g. Best et al. 2006; Bower et al. 2006; Croton et al. 2006) has shown that the extended radio sources have a significant impact on the hot gas on cluster scales through feedback effects (e.g. the quenching of cooling flows in massive haloes). Hence, a significant contribution to the overall AGN feedback from the young, expanding radio sources on smaller scales should be expected. Indeed, over the last few years, fast nuclear outflows (up to $\sim$2000 km s^{-1}) have been detected in a number of compact (young) radio sources, both in the optical emission lines (e.g. Tadhunter

⋆E-mail: jholt@strw.leidenuniv.nl

et al. 2001; Holt, Tadhunter & Morganti 2003; Holt et al. 2006, 2008; the latter 3 references: H03, H06 & H08 hereafter) and in neutral hydrogen as deep absorption features (e.g. Morganti et al. 2003, 2004; Morganti, Tadhunter & Oosterloo 2005).

In H08, we reported results for the emission-line kinematics in a complete sample of 14 compact radio sources, including both compact steep spectrum (CSS) radio sources (size $<$15 kpc) and gigahertz-peaked spectrum (GPS) radio sources (size $<$1 kpc). The observed line widths and blueshifts (up to $\sim$2000 km s^{-1}) in the nuclear emission-line gas are too large to be explained by gravitational motions. Instead, the extreme kinematics were interpreted as signatures of strong interactions between the young, small-scale radio jets and the emission-line gas, following the model proposed for PKS 1549−79 by Tadhunter et al. (2001). This interpretation is supported by evidence for strong radio-optical alignments in *all* CSS sources with deep *Hubble Space Telescope* (*HST*) imaging, including some sources in this sample (e.g. de Vries et al. 1997, 1999; Axon et al. 2000; Privon et al. 2008).

Although the expanding radio jets provide a convenient outflow driving mechanism, consistent with the results on the emission-line kinematics, it is important to test this scenario further. In this paper, we use optical emission-line ratios (from the line modelling in H08) to investigate the physical conditions and the dominant ionization mechanism(s) of the narrow-line gas, in particular to determine whether the emission-line regions are shocked, as expected in the case that the outflows are being accelerated by jet–cloud interactions (e.g. Clark et al. 1998; Villar-Martín et al. 1998; Solórzano-Iñarrea et al. 2001). In Section 2, we give a brief overview of the sample, observations, data reduction and analysis techniques and refer the reader to H08 for a detailed discussion. In Section 3, we discuss the line fluxes and, in particular, the reddening, density and temperature of the emission-line gas, giving brief details of the line modelling. We discuss the line ratios in detail in Section 4, along with diagnostic diagrams and radio-optical correlation plots. All line fluxes, aperture information and extracted nuclear spectra are presented in the Appendices. Information on the emission-line kinematics for all sources is presented in H08.

Throughout this paper, we assume the following cosmology: $H_0 = 71$ km s^{-1}, $\Omega_0 = 0.27$ and $\Omega_\Lambda = 0.73$.

2 SAMPLE SELECTION, OBSERVATIONS, DATA REDUCTION AND ANALYSIS TECHNIQUES

This paper is the second in a series of two reporting deep optical spectroscopic observations of a complete sample of compact radio sources. Below we summarize the important points and refer readers to H08 for a detailed description of the sample, observations, data reduction and analysis techniques.

Our complete sample comprises 14 compact radio sources derived from the northern 3C and 4C samples and southern 2 Jy sample and includes eight CSS, three GPS, two compact core sources and one compact flat-spectrum source. The sample has intermediate redshifts ($z < 0.7$) and a radio power range of $26 < \log P_{5\,\mathrm{GHz}} < 28$ (W Hz^{-1}).

Long-slit optical spectroscopic observations of the full sample were obtained during three observing runs with ISIS/WHT, EMMI/NTT and FORS2/VLT. In order to include the outflowing regions in the slit, and to ensure the spectra were of sufficient resolution, the observations were made using a 1.0–1.5 arcsec slit, while to reduce the effects of differential atmospheric refraction, all objects were observed either at low airmass (sec $z < 1.1$) and/or with the slit aligned along the parallactic angle. Due to various observational constraints, we have only aligned the slit along the radio axis for approximately half of the sources. For full details of the observational setup, we refer readers to table 2 of H08.

The data were reduced in the usual way (bias subtraction, flat fielding, cosmic ray removal, wavelength calibration, flux calibration) using the standard packages in IRAF. To ensure good flux calibration ($\pm$5 per cent), several spectrophotometric standard stars were observed during each run with a wide (5 arcsec) slit. This accuracy was confirmed by good matching in the flux between the red and blue spectra.[1] Additional standard stars were observed with a narrow slit to correct the spectra for atmospheric absorption features (e.g. *A* and *B* bands). The spectra of all sources were corrected for Galactic extinction using the $E(B-V)$ values from Schlegel, Finkbeiner & Davis (1998) and the Seaton (1979) extinction law. The wavelength calibration accuracies were 0.06–0.53, 0.06–0.24 and 0.20–0.24 Å for the WHT, NTT and VLT data, respectively, dependent on wavelength range. Similarly, the spectral resolutions were typically 3.3–4.8 $\pm$ 0.2 Å, 4.3–6.7 $\pm$ 0.1 Å and 6.5–7.4 Å for the WHT, NTT and VLT data, again dependent on wavelength range. The spatial resolutions were 0.36, 0.33 and 0.25 arcsec pixel^{-1} for the WHT, NTT and VLT data, respectively. The seeing range was 0.8–2.5 arcsec. Full details are given in table 2 of H08.

As discussed in H08, in order to detect and accurately model the broader emission-line components, it is necessary to model and subtract the underlying continuum emission. For the broader, blueshifted emission-line components, variations in the continuum can make it difficult to establish the centroid, full width at half-maximum (FWHM) and line flux of the Gaussian. If the underlying continuum also contains strong stellar absorption lines (e.g. Hβ, etc), a good model of the continuum is required to ensure that the emission-line fluxes are accurately modelled. Holt (2005) estimated that subtracting different continuum models which all provided a reasonable fit to the spectral energy distribution (SED) can cause a difference of up to 10 per cent in the flux in the broader components, although typically the narrower components are less affected.

As a first step in modelling the continuum, we generated and subtracted the nebular continuum following Dickson et al. (1995), taking full account of reddening following the techniques outlined in H03. The remaining continuum was then modelled using a customized IDL minimum χ^2 fitting program (see e.g. Robinson 2001; Tadhunter et al. 2005; Holt et al. 2007 for details) allowing up to three separate continuum components: 12.5 Gyr unreddened old stellar population (OSP), a young stellar population (YSP) with reddenings $0 < E(B-V) < 1.6$ and age $0.01 < t_{\mathrm{YSP}} < 5.0$ Gyr, and an AGN/power-law component. The best-fitting model, defined as that with the least number of components required to adequately model both the overall SED and discrete stellar absorption features (e.g. Ca H+K, Balmer series), was then subtracted. The continua of three sources were not modelled in this way: 3C 277.1 (quasar), PKS 1814−63 (foreground star) and 3C 303.1 (mismatching of the blue and red spectra). Full details of the subtracted models can be found in H08.

The spectra were extracted and analysed using the STARLINK packages FIGARO and DIPSO. Note that some components for a few key diagnostic lines were not detected in some apertures. For these, we have estimated upper limits for the flux by adding Gaussians to

[1] The only exception was 3C 303.1. For this source, the only ratio data used is for lines observed with the same arm of the ISIS spectrograph.

the data until the line component could just be detected on visual inspection of the spectra.

Throughout this paper, we use the kinematic component definition defined in H08:

(i) narrow: FWHM < 600 km s^{-1};
(ii) intermediate: $600 <$ FWHM < 1400 km s^{-1};
(iii) broad: $1400 <$ FWHM < 2000 km s^{-1}; and
(iv) very broad: FWHM > 2000 km s^{-1}.

3 RESULTS

As discussed above, the nuclear emission lines in compact radio sources are often broad, with asymmetric profiles requiring multiple Gaussian components to model them. In H08, we modelled the nuclear emission lines for all sources in our sample, identifying between 2 and 4 Gaussian components with velocity widths and blueshifts of up to 2000 km s^{-1}. Here, we use the emission-line models from H08 and focus our analysis on the emission-line fluxes and ratios. We use emission-line ratios and diagnostic diagrams to investigate whether the compact radio sources in our sample still retain their dense and dusty natal cocoons (reddening and emission-line density), and to investigate the dominant ionization mechanism(s) and the implications for the likely outflow driving mechanism. For brevity, the line fluxes of all lines in all apertures extracted are presented in Appendix A.

3.1 Aperture extraction and emission-line modelling

For a detailed discussion of the emission-line modelling, we refer readers to H08 and we only summarize the key points here.

3.1.1 Aperture selection

In H08, with the exception of modelling the most extended emission lines in the spatial direction to accurately determine the systemic velocities, the main results on the emission-line kinematics were derived from wide nuclear apertures centred on the nuclear continuum emission. These nuclear apertures, which also form the basis of the analysis in this paper, are shown in Appendix B along with spatial profiles of the bright emission lines and the continuum emission, and the full extracted nuclear spectra. In addition, five sources (3C 268.3, 3C 277.1, PKS 1345+12, PKS 1814−63 and 3C 459) show evidence for extended emission in several lines and we have extracted further apertures. The positions of these, along with the extracted spectra, are also shown in Appendix B.

3.1.2 Emission-line modelling

In general, we have modelled all emission lines in a particular aperture using a kinematic model derived from the [O III]$\lambda\lambda$4959,5007 doublet, a standard technique for modelling the emission lines in radio galaxies. In short, the velocity widths and shifts of the various components were fixed to be the same as for the [O III] doublet, with further constraints arising from atomic physics. As all lines can be reproduced by the same model, we can assume with confidence that the emission originates from similar regions of the ISM. Hence, it is meaningful to use emission-line ratios to investigate the physical and ionization properties of the emission-line gas.

Notable exceptions are the nuclear apertures of the GPS sources PKS 1345+12 and PKS 1934−63. For these apertures, one model did not reproduce all lines. In these latter cases, only components consistent in all lines (e.g. the narrow components in PKS 1345+12) are plotted in the diagnostic diagrams. Finally, for 3C 303.1, we only consider line ratios from lines in the same arm of the instrument, as the two arms do not match in flux.

3.2 Emission-line densities

During the early stages of radio source evolution, the nuclear regions of radio sources are likely to harbour a rich ISM, deposited during the activity triggering event. Here, we investigate the density of the circumnuclear gas using the [S II] 6716/6731 density diagnostic ratio. The measured ratios were converted to densities using the IRAF program TEMDEN, part of the STSDAS package, which is based on the five-level atom calculator developed by de Robertis, Dufour & Hunt (1987). For all calculations, we have assumed an electron temperature of $T_e = 10\,000$ K, although the [S II] ratio varies little with temperature. As discussed above, when modelling the emission lines in the nuclear aperture of each source, the profiles of all lines were well fitted by the corresponding [O III] model. The only exceptions were PKS 1345+12 (discussed in detail in H03) and PKS 1934−63.

The derived electron densities are summarized in Table 1. In the nuclear apertures, we have been able to accurately determine the electron density for five components only: 3C 213.1 (narrow), 3C 303.1 (intermediate), PKS 0023−26 (narrow), PKS 1934−63 (narrow) and 3C 459 (narrow). For the remaining components, we have only been able to determine whether the components are consistent with low or high density. The reason for this is that the blend is highly complex, requiring four to eight Gaussian components (2–4 per line) for an adequate fit, and the velocity widths and shifts of the broader components are often comparable to the separation of the lines in the doublet (see Fig. 1 and also H03); it is usually possible to confidently determine the *total flux* in, for example, the broad components together, but to determine the density the ratio is required. Hence, whilst the [O III] model generally provides a good fit to the [S II] doublet, in many cases it is not possible to obtain a *physically viable* good fit without forcing the 6716/6731 ratio to the high (0.44) or low (1.42) density limit of the diagnostic.

Although we have not been able to accurately measure the electron densities in the majority of apertures, from the results presented in Table 1, we can draw the following general conclusions:

(i) The nuclear narrow components tend to be consistent with low electron densities (few hundred cm^{-3}), as do the extended narrow components.

(ii) The nuclear broader components (intermediate/broad/very broad) appear to be consistent with higher densities ($n_e >$ 10^3 cm^{-3}).

3.3 Reddening

In Section 3.2, and also in H03, we showed that there is a suggestion that the nuclear regions of our sample of compact radio sources may harbour a dense ISM ($n_e >$ few 1000 cm^{-3}). Observationally, in addition to high densities, large amounts of gas and dust can also be detected as reddening of the optical spectrum.

We have investigated reddening in all apertures in our sample using the Balmer line ratios (e.g. Hα/Hβ, Hγ/Hβ and Hδ/Hβ), assuming a simple foreground screen model for interstellar dust (Seaton 1979). The corresponding $E(B-V)$ values for each object/aperture are summarized in Table 1.

Table 1. Summary of the physical conditions (density, reddening and temperature) for the sample.

Object	Aperture	Electron density, n_e (cm^{-3})					$E(B-V)$ value				
		n	i	b	vb		n	i	b	vb	
(a)	(b)	(c)	(d)	(e)	(f)	(g)	(h)	(i)	(j)	(k)	(l)
3C 213.1	nuc	480^{+180}_{-150}	–				Zero	>0.2			[c]
3C 268.3	nuc	1.42[b]/1.42[a]	1.42[b]				Zero/zero	$0.7^{+0.1}_{-0.1}$			[c]
	SE	1.42[a]					Zero				
	NW	–					$0.6^{+0.3}_{-0.2}$				
3C 277.1	nuc	<600	0.44[b]				Zero	$0.7^{+0.3}_{-0.4}$		BLR: zero	[c]
	SE blob	–/–					Zero/zero				
	SE HII	–					Zero				
4C 32.44	nuc	–/–		–	–		Zero/zero		$0.9^{+0.1}_{-0.1}$	$1.0^{+0.3}_{-0.6}$	[c]
PKS 1345+12	nuc	1.42[b] (<150)	>5300	>4200		[c]	Zero	$0.4^{+0.1}_{-0.1}$	$1.4^{+0.5}_{-0.5}$		[c]
	NW, PA160	500^{+300}_{-200}					Zero				
	SE, PA160	1.42[a]/1.42[b]					$0.5^{+0.1}_{-0.1}$/$1.2^{+0.4}_{-0.7}$				
	NE, PA230	1.42[a]					$0.7^{+0.2}_{-0.3}$				
	SW, PA230	–/1.42[a]					–/$0.7^{+0.1}_{-0.1}$				
3C 303.1	nuc	1.42[b]	110^{+40}_{-40}			[c]?	Zero	$0.5^{+0.2}_{-0.2}$			[c]
PKS 0023−26	nuc	400^{+200}_{-150}	1.42[a]				Zero	Zero			
PKS 0252−71	nuc						Zero/zero	Zero			
PKS 1306−09	nuc						Zero/zero				
PKS 1549−79	nuc	1.42[a]	0.44[b]				Zero	Zero		BLR: $2.8^{+0.1}_{-0.1}$	
	PA75	1.42[a]	0.44[b]				$0.4^{+0.1}_{-0.1}$	$0.4^{+0.1}_{-0.2}$			
	PA5	1.42[a]					–				
PKS 1814−63	nuc	1.42[a]/700^{+150}_{-150}					–/–				
	ext	240^{+100}_{-90}									
PKS 1934−63	nuc	600^{+300}_{-200}		0.44[b]			Zero				
PKS 2135−20	nuc		–/–					Zero/$1.3^{+0.4}_{-0.2}$			
3C 459	nuc	300^{+100}_{-100}		0.44[b]			Zero		$1.3^{+0.1}_{-0.1}$		[c]
	ext	1.42[b]		1.42[b]			Zero		Zero		

Note that, as discussed in Section 2 and H08, many galaxies in the sample exhibit stellar absorption features. Whilst the continuum modelling and subtraction attempts to remove these features, if a weak Balmer emission line is coincident with a strong absorption feature (e.g. Hδ and, to a lesser extent, Hγ), this may result in an incorrect (large) estimate of the reddening. When modelling and subtracting the continuum (see H08), the effect of the underlying absorption lines on the emission lines was investigated, focussing in particular on the different components of Hβ. The well-defined narrow components of the emission lines are often relatively unaffected by the subtraction of different models. However, the flux in the broader components could be affected by as much as 10 per cent or more. Hence, wherever possible, estimates of reddening from the stronger Balmer lines are used. It should also be noted that in the more extreme sources, with several components to the emission lines, there is also difficulty in accurately modelling Hα due to the complexity of the blend with the [N II] doublet. Fig. 2 demonstrates this for the nuclear aperture of PKS 1549−79.

The degree of estimated reddening varies over a wide range, from negligible to highly extinguished. There does not appear to be any particular trend with radio source size (i.e. GPS or CSS), although some of the highest $E(B-V)$ values are measured in the GPS sources [e.g. $E(B-V)=1.0$ in 4C 32.44 and $E(B-V)=1.4$ in PKS 1345+12]. The main trend appears to be the increase in reddening with the FWHM of the emission-line component *within* a particular object. In 7/14 sources (denoted by the stars in Table 1), the degree of reddening increases significantly from the narrow component, often suffering negligible reddening (although some objects exhibit narrow components with moderate reddening), to the intermediate and broad components where reddening is almost always significant. This effect was first observed in the GPS source PKS 1345+12 and is discussed by H03. Of the remaining seven objects which do not show this effect, it is not possible to do this test in two sources (i.e. both components observed have similar FWHM as in PKS 1306−09) and in one further object, PKS 1814−63, the degree of reddening is not estimated. Taking this into account, 7/11 sources (or 67 per cent) show the trend of increasing reddening with increasing FWHM. Hence, all reddening estimates are consistent with dense and dusty cocoons surrounding the young radio sources, and in more than half of the sources observed, there is strong evidence for stratification of the ISM as in PKS 1345+12. Such strong reddening in the nuclear regions of radio sources is not uncommon and is observed in a number of extended radio sources such as Cygnus A (Tadhunter, Shaw & Morganti 1994b; Taylor, Tadhunter & Robinson 2003).

Whilst we can see the general trends in the reddening, and draw conclusions about the existence of a dense and dusty circumnuclear cocoon, given the various uncertainties discussed above, we have not corrected the line fluxes for reddening. For some line ratios (e.g. [S II] for the density), the lines are close together and reddening effects will be negligible. For the diagnostic diagrams presented later, for ratios in which the lines have a large separation in wavelength, we plot the uncorrected values.

Table 1 – *continued*

Object	Aperture	Electron temperature, 10^3 T_e (K)			
		n	i	b	vb
(a)	(b)	(m)	(n)	(o)	(p)
3C 213.1	nuc	<19	<30		
3C 268.3	nuc	$16^{+8}_{-3}/15^{+4}_{-2}$	18^{+18}_{-4}		
	SE	18^{+1}_{-1}			
	NW	–			
3C 277.1	nuc	25^{+1}_{-1}	50^{+100}_{-20}		
	SE blob	<35/<55			
	SE HII	<95			
4C 32.44	nuc	11^{+6}_{-2}/<18		<13	<70
PKS 1345+12	nuc				
	NW, PA160	14^{+3}_{-2}			
	SE, PA160				
	NE, PA230				
	SW, PA230				
3C 303.1	nuc	<16	15^{+2}_{-1}		
PKS 0023−26	nuc	22^{+5}_{-3}	<35		
PKS 0252−71	nuc	$32^{+20}_{-10}/30^{+80}_{-10}$	110^{+100}_{-60}		
PKS 1306−09	nuc	$90^{+40}_{-90}/40^{+40}_{-10}$			
PKS 1549−79	nuc	14^{+4}_{2}			
	PA75				
	PA-5				
PKS 1814−63	nuc				
	ext				
PKS 1934−63	nuc				
PKS 2135−20	nuc	10^{+1}_{-1}	<18		
3C 459	nuc	<46	<66		
	ext				

Note. Where there are two components with similar FWHM (i.e. two narrow components), the component at the systemic velocity is presented first (for PKS 1306−09 the blue narrow component is presented first); n = narrow; i = intermediate; b = broad; vb = very broad.

Blank positions in the table indicate kinematic components not observed in a source/aperture. For components which are not detected in a relevant diagnostic line, the entry is '–'.

[a]Was measured and found to be consistent with either the low-density limit ([S II]λ6716/λ6731 = 1.42) or the high-density limit ([S II]λ6716/λ6731 = 0.44), within the uncertainties.

[b]Forced to the low (1.42) or high (0.44) density limit. See text for details.

[c]Sources in which there is a clear trend of increasing density (column g) or reddening (column l) with FWHM.

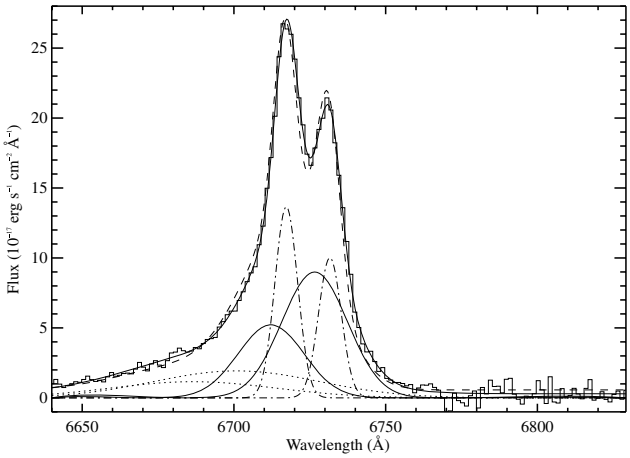

Figure 1. The [S II]λλ6716,6731 doublet in the nuclear aperture of PKS 1345+12 (taken from H03). The faint solid line (histogram) represents the data, the bold line is the overall best-fitting model to the doublet, the dashed line is the [O III] model to the [S II] doublet and the dot–dashed, solid and dotted pairs of lines are the narrow, intermediate and broad components. This plot highlights the difficulties in obtaining a unique model for the [S II] doublet. Although it is relatively straightforward to fit the correct number of components, and we can confidently determine the *total flux* in, for example, the intermediate or broad components, the widths and shifts of the broader components are comparable to the separation of the lines in the doublet. This makes it difficult to determine the ratio between the two intermediate or two broad components, which is critical for determining the density.

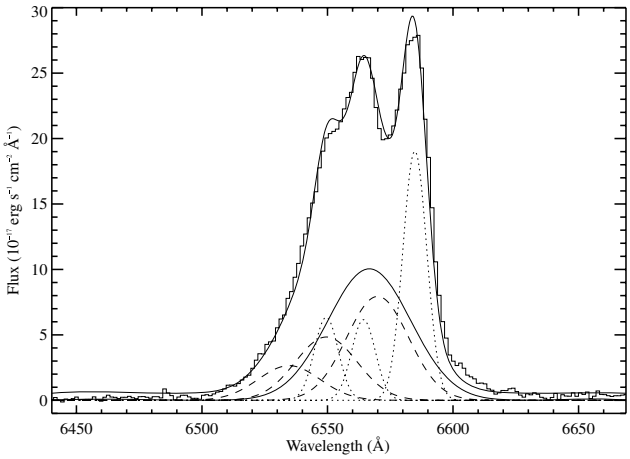

Figure 2. The Hα,[N II]λλ6548,6584 blend in the nuclear aperture of PKS 1549−79. The faint solid line (histogram) is the data, the bold line is the overall best-fitting model to the doublet and the dotted and dashed lines are the narrow and intermediate components (three of each: one from Hα and two for [N II]). The solid Gaussian is the broad component detected only in Hα in the optical (see H06 for details). This plot highlights the complexity of the Hα/[N II] blend and the difficulties in measuring the reddening using Hα/Hβ ratio.

3.4 Electron temperature

The electron temperature can be an important diagnostic for distinguishing between the different ionization mechanisms. For example, one would expect to observe higher temperatures if the gas is shock ionized rather than photoionized by the AGN.

The electron temperature, T_e, can be derived from the temperature diagnostic [O III](4959 + 5007)/4363. Where the weaker [O III]λ4363 line is detected, we have calculated the electron temperature, assuming an electron density of 10^3 cm^{-2}. The derived electron temperatures are summarized in Table 1.

No clear trends are observed across the entire sample but *all* measured temperatures are relatively high (in the main $\gtrsim$14 000 K), and in some objects (e.g. 4C 32.44) a gradient with FWHM is observed, although the uncertainties are large. Such temperatures are too high to be accounted for by simple single slab photoionization models which generally predict temperatures of $\lesssim$11 000 K (Tadhunter, Robinson & Morganti 1989) and may be a signature of shock ionization, although mixed-medium ionization models could also account for such high temperatures (Binette, Wilson & Storchi-Bergmann 1996). Density effects may also be responsible for the unrealistically high temperatures measured in some sources/apertures.

4 DISCUSSION

4.1 Do compact radio sources harbour a dense and dusty natal cocoon?

Tadhunter et al. (2001) concluded that the compact, flat spectrum radio source PKS 1549−79 is a young, recently triggered radio-loud AGN which is still surrounded by a dense and dusty natal cocoon, obscuring the active nucleus from view. This was confirmed by the detection of the proto-quasar, initially at near-infrared wavelengths (Bellamy et al. 2003) and, later, at the reddest optical wavelengths in higher quality optical spectra (H06). Deep optical images also reveal that PKS 1549−79 has recently been involved in a major merger event. Similarly, H03 reported the discovery of significant reddening and high electron densities in the nuclear aperture of the GPS source PKS 1345+12. Again these results were interpreted as the signature of a dense and dusty natal cocoon, particularly as PKS 1345+12 also shows evidence of a recent merger (double nucleus in a common envelope, e.g. Axon et al. 2000).

In Sections 3.2 and 3.3, we investigated the density and reddening in the nuclear apertures of 14 compact radio sources, including PKS 1345+12 and PKS 1549−79. Whilst it has been difficult to obtain unique results, particularly for the electron densities, we can draw some general conclusions. The majority of the sources in the sample do tend to show evidence for high densities and large reddening in the nuclear regions, particularly in the broader shifted components. This trend is particularly apparent in the reddening – 7/14 sources show convincing evidence for increasing reddening with FWHM (two GPS, three CSS and two compact core sources).

Hence, it is clear that the nuclear regions of compact radio sources contain large amounts of gas and dust. This is consistent with the large reddening observed in the optical spectra of CSS quasars (Baker & Hunstead 1995), although at X-ray wavelengths, the evidence for differences in column densities between young AGN and more extended radio sources is contradictory. Guainazzi et al. (2006) report high column densities in GPS sources, for all sources in their small sample with good quality hard X-ray data. The measured column densities in GPS sources are higher compared to FR I and BLR FR II sources, but comparable to high-ionization FR II sources, and so they suggest the obscuring material is located in an obscuring torus. However, Vink et al. (2006) find a variety of column densities in GPS and CSS sources, with no evidence for higher column densities compared to more extended radio sources. This latter observation is consistent with the fact that strong optical reddening is not uncommon in the nuclear regions of extended radio sources (e.g. Robinson et al. 1987; Tadhunter et al. 1994a; Robinson et al. 2000; Robinson 2001; Taylor et al. 2003).

Whilst there is evidence for a dense and dusty circumnuclear cocoon, there appears to be insufficient material to constrain and frustrate the radio sources (e.g. PKS 1345+12: H03). The only way frustration would be possible is if the matter were distributed in giant clouds, which may be able to disrupt a radio jet (Bicknell et al. 2003). Hence, the observations are consistent with compact radio sources being young, recently triggered radio sources residing in dense and dusty natal cocoons, rather than old, confined and frustrated radio sources.

4.2 What is the dominant ionization mechanism for the gas?

Tadhunter et al. (2001) suggested that the outflow in the compact radio source PKS 1549−79 is driven by the expanding radio jets. Certainly, jet-driven outflows are a convenient way of explaining the extreme kinematics observed in the optical emission-line gas. However, it is also possible that the outflows have been accelerated by some other mechanism, for example, quasar-induced winds or starburst driven superwinds.

A key way to try to distinguish between these scenarios is the use of emission-line ratios and diagnostic diagrams, a technique successfully employed for identifying jet–cloud interactions in the extended emission-line regions (EELRs) of extended radio sources (e.g. Clark et al. 1998; Villar-Martín et al. 1998; Solorzano-Iñarrea 2001). We have, therefore, plotted a variety of diagnostic diagrams for the different emission-line components in Fig. 3 (nuclear narrow and extended components) and Fig. 4 (nuclear broader/shifted components). In addition to the data for this sample, we have also plotted a comparison sample of nearby extended radio galaxies with detailed line ratio information (see the caption of Fig. 3 for details) and model results for simple slab AGN photoionization (from MAPPINGS Ic: see Ferruit et al. 1997), mixed-medium photoionization (Binette et al. 1996) and the latest shock and shock plus precursor models from Allen et al. (2008). Full details of the models are given in the caption of Fig. 3. Note that it can be difficult to distinguish between the AGN and shock plus precursor models for the high shock velocity case, because the hard continuum generated in the hot post-shock gas (that photoionizes the precursor) can mimic that of an AGN nucleus. Moreover, the mixed medium models of Binette et al. (1996), while successfully explaining the relatively strong high ionization lines and high electron temperatures measured in some AGN, cover only a limited range of parameter space for the matter- and radiation-bound components included in the models; better agreement with the observed line ratios in a given object might be obtained by tuning the input parameters of such models.

Initial inspection of Figs 3 and 4 reveals that the positions of the broader and narrower emission-line components of the compact radio sources are not significantly different from each other, and are remarkably similar to those of the comparison sample of extended radio sources. This latter result is surprising given the striking differences in the nuclear emission-line kinematics and the strong radio-optical alignments reported for CSS sources (see Section 4.3).

In terms of the results for the compact radio sources, whilst the diagrams are complex, it is still possible to identify some tendencies in the data when interpreting all diagrams together:

(i) *Narrow components.* In the majority of the diagrams (e.g. Figs 3a, b and e), the nuclear narrow components lie close to tracks for photoionization (both simple AGN photoionization and the $A_{M/I}$ sequence) whilst in Figs 3(c) and (d), the nuclear narrow components lie away from the plotted photoionization tracks, and appear more consistent with shock models. However, in the latter cases, the data always lie closer to the higher velocity end of the tracks ($v_{\rm shock} \geq 500\,{\rm km\ s^{-1}}$). Given that the nuclear narrow components are relatively quiescent, with small velocity widths (FWHM $\lesssim 400\,{\rm km\ s^{-1}}$), and no blueshifts (H08 demonstrated that they are at the systemic velocity), such an interpretation would be unlikely. It should also be noted that, in both Figs 3(a) and (b), the locus of the data for the narrow components is similar to that for the mixed-medium photoionization models – varying the parameters of the mixed-medium models would result in tracks which describe the data better than the other models. We, therefore, interpret Fig. 3 as the nuclear narrow components showing a tendency to be consistent with AGN photoionization (both simple slab and mixed-medium models). The extended narrow components are also

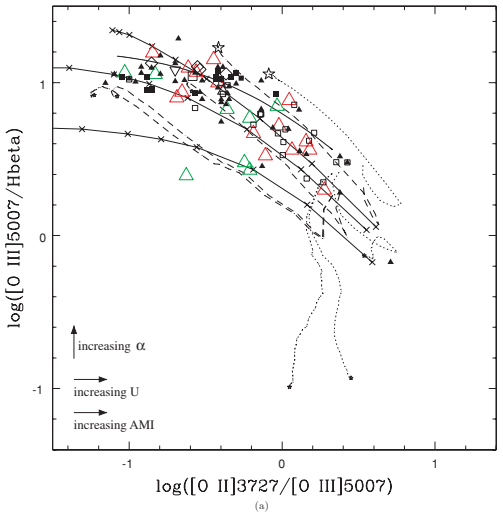

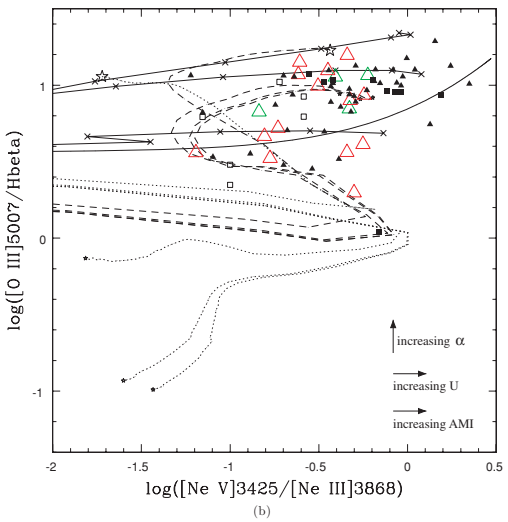

Figure 3. Diagnostic diagrams for the entire sample of nuclear narrow components (large red open triangles) and extended components (large green open triangles). Arrows represent upper limits. The ionization models plotted are as follows. Crosses joined by solid black lines: optically thick power-law (AGN) photoionization sequence in the ionization parameter U ($2.5 \times 10^{-3} < U < 10^{-1}$) from MAPPINGS for $\alpha = -1.0, -1.5$ q and -2.0. Bold black solid line: mixed-medium models (including both matter-bound and ionization-bound clouds; $10^{-2} \leq A_{M/I} \leq 10$) from Binette et al. (1996). Dotted lines: new shock models from Allen et al. (2008). Sequences are for magnetic paramter, $B/\sqrt{n} = 0.01, 1, 10, 100, 1000$ μG cm$^{3/2}$, with shock velocities 10^2–10^4 km s^{-1} and pre-shocked gas density $n_e = 100$ cm^{-3}. The stars identify the highest shock velocity (10^4 km s^{-1}) on each track with the large open star identifying the track with the highest magnetic paramter. Ddashed lines: new shock plus precursor models from Allen et al. (2008). Sequences are for magnetic paramter, $B/\sqrt{n} = 0.01, 1, 10, 100, 1000$ μG cm$^{3/2}$ with shock velocities 10^2–10^4 km s^{-1} and pre-shocked gas density $n_e = 100$ cm^{-3}. The stars identify the highest shock velocity (10^4 km s^{-1}) on each track with the large open star identifying the track with the highest magnetic paramter. For comparison, various data from the literature are overplotted (small black points): nuclear regions (filled triangles: Costero & Osterbrock 1977; Grandi & Osterbrock 1978; Cohen & Osterbrock 1981; Robinson et al. 1987; Tadhunter 1987; Storchi-Bergmann et al. 1996; Dickson 1997; Clark et al. 1998; Villar-Martín et al. 1998; Robinson et al. 2000; Solorzano-Iñarrea 2001; Wills et al. 2002); EELRs (filled squares: Morganti et al. 1991; Tadhunter et al. 1994b; Storchi-Bergmann et al. 1996; Robinson et al. 2000); EELRs with evidence for jet–cloud interactions (open squares: Clark et al. 1998; Villar-Martín et al. 1998; Solorzano-Iñarrea 2001); and all regions in Cygnus A (larger black open symbols: Taylor et al. 2003).

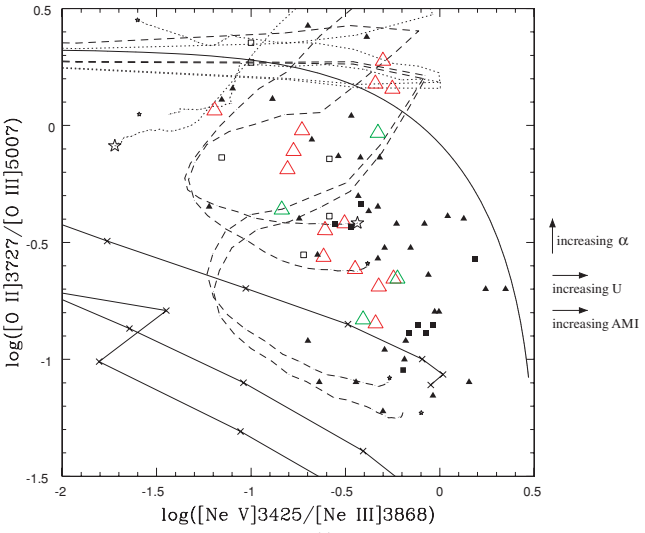

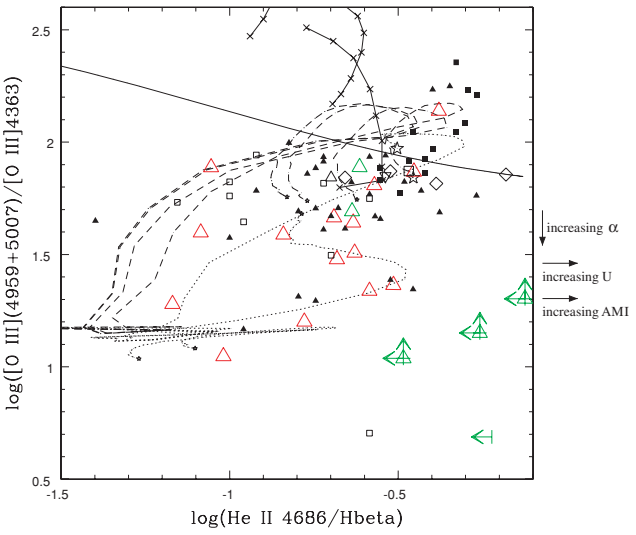

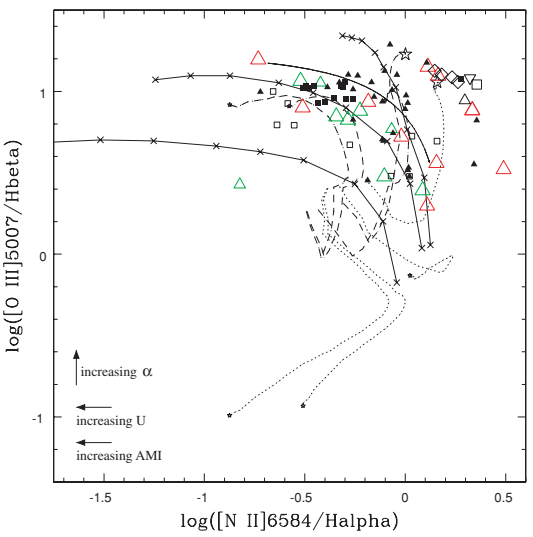

Figure 3 – *continued*

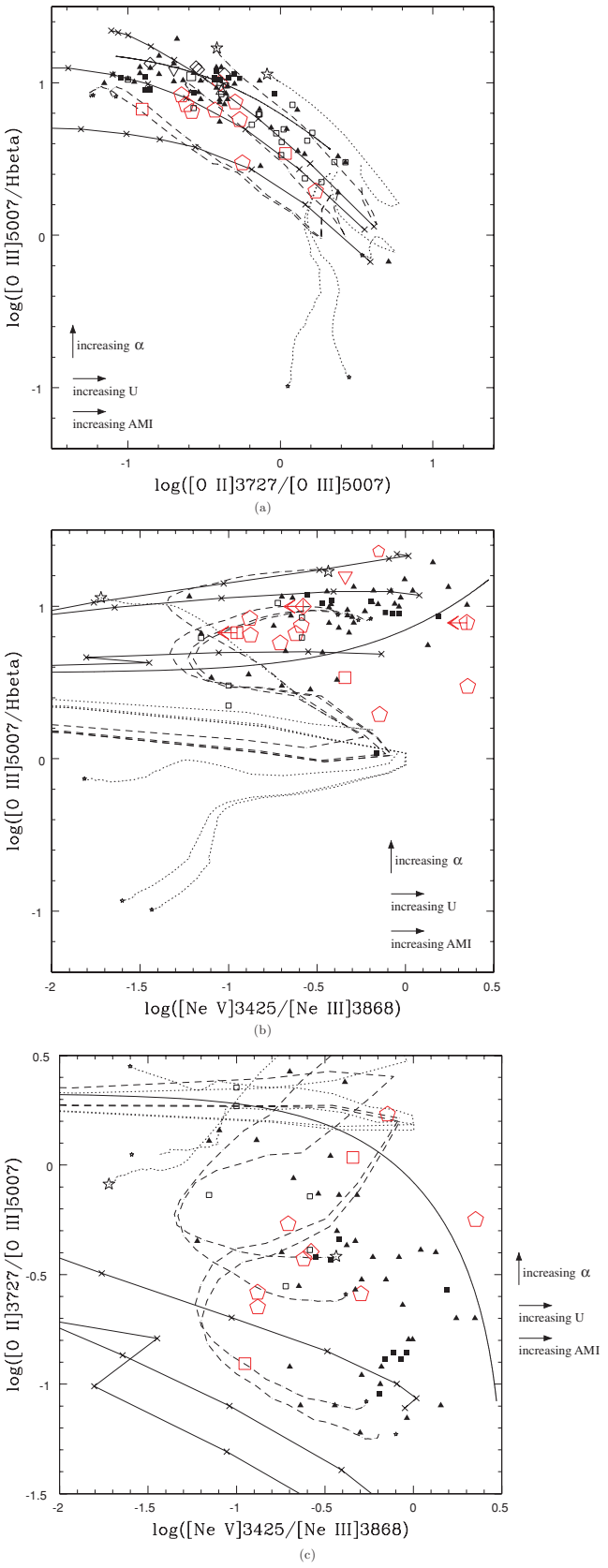

Figure 4. Same as for Fig. 3, but for the shifted components: intermediate (red open pentagons), broad (red large open squares) and very broad (red large open diamonds). Small black points represent the comparison sample (see caption of Fig. 3 for details).

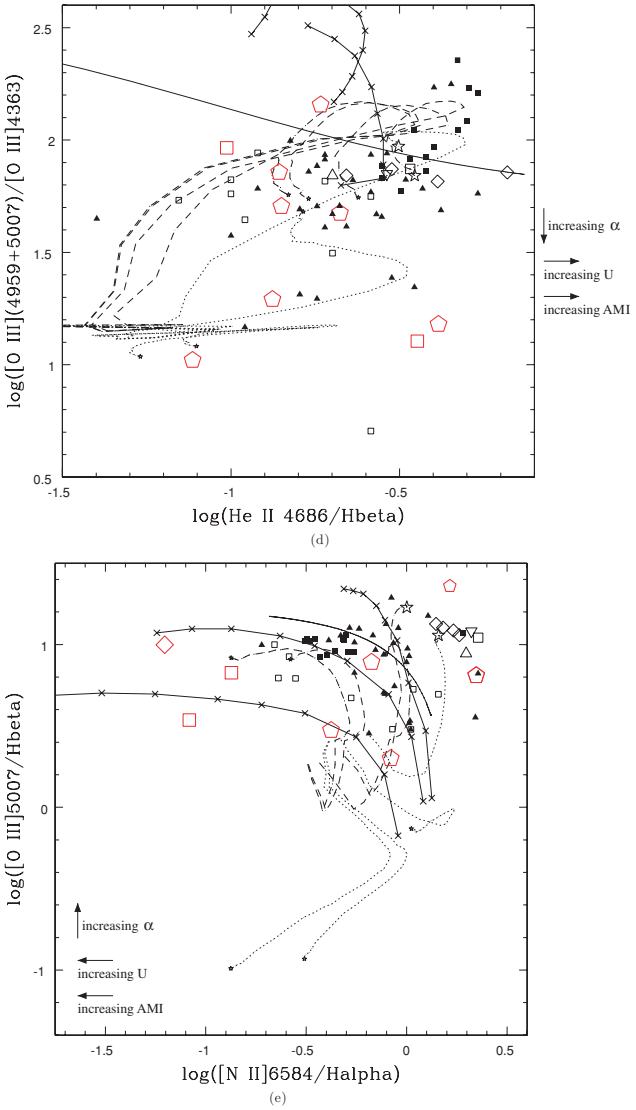

Figure 4 – *continued*

plotted on Fig. 3, and we see no significant differences between the nuclear and extended narrow components, suggesting they have similar ionization mechanisms.

(ii) *Broad, shifted components.* As for the nuclear narrow components, careful consideration of all information together, along with details of the models, is required in order to disentangle the overlapping models on the diagnostic diagrams in Fig. 4. From all the diagrams in Fig. 4, we can rule out pure shock ionization. In all five panels of Fig. 4, the data occupy the same region as the shock plus precursor models, typically in the region of high-velocity ($v_{\rm shock} \gtrsim 500$ km s^{-1}) shocks (this is most clearly seen in e.g. Figs 4a–c). In some diagrams, the location can also be interpreted as consistency with AGN photoionization (e.g. Figs 4a and b), but in Figs 4(c) and (d), the data are neither in the same region nor have the same loci, as any of the photoionization models. Again, by combining all diagrams, there appears to be a mild tendency towards shock plus precursor models, with high shock velocities ($v_{\rm shock} \gtrsim 500$ km s^{-1}) in the nuclear shifted components, although this evidence is not conclusive.

(iii) *Object classification*. The [O III]λ5007/Hβ versus [N II]λ6584/Hα diagram (Figs 3e and 4e for the narrow and broad components, respectively) is a well-known diagram to distinguish between the different classes of object and, therefore, the dominant ionization mechanism (e.g. Kewley et al. 2001; Kauffmann et al. 2003). Almost all components are consistent with AGNs/Seyferts, with a few in the region of the diagram occupied by LINERS. There are a couple of notable exceptions – the extended region to the south-east (SE) of the nucleus in 3C 277.1, and the extended regions to the SE and south-west (SW) in PKS 1345+12 are all consistent with stellar photoionization. The observation of ongoing star formation in radio galaxies is rare, with only a few other cases known: e.g. Coma A (Solórzano-Iñarrea & Tadhunter 2003); PKS 1932−46 (Villar-Martín et al. 2005). The super star clusters (SSCs) in the halo of PKS 1345+12 are discussed in Rodriguez Zaurin et al. (2007).

4.3 What drives the outflows?

In H08, we reported evidence for extreme emission-line outflows in the nuclear regions of 11/14 compact radio sources. From the kinematics alone, the large velocity shifts and widths (FWHM) observed (up to 2000 km s^{-1}) are entirely consistent with the idea that the young, expanding radio source is strongly interacting with the natal cocoon and driving outflows in the ISM, as suggested by the results for PKS 1549−79 (Tadhunter et al. 2001). This argument is further strengthened by the growing evidence in the literature that the line emission in CSS sources is both on similar scales to, and often closely aligned with, the radio source (de Vries et al. 1997; de Vries et al. 1998; Axon et al. 2000). This effect is observed for *all* CSS sources with *HST* imaging. Recent *HST* imaging of two of the sources in our sample (PKS 1345+12 and PKS 1549−79) by Batcheldor et al. (2007) has also shown that in the smaller GPS sources, the optical line emission is also on a similar scale to the radio source. However, although galaxy wide outflows (i.e. starburst-driven winds) can be confidently ruled out for GPS sources, on the basis of emission-line region morphology it is not possible to distinguish between AGN winds and jet–cloud interactions, which would both be expected on the nuclear scales.[2] Whilst the kinematics and radio-optical alignments are clearly suggestive of jet–cloud interactions and radio jet-driven outflows, the above evidence alone is, so far, circumstantial.

In this paper, we have attempted to address this problem using optical emission-line ratios and diagnostic diagrams. In Sections 3.2 and 3.4, we measured electron densities and temperatures. Although we measure large densities and high temperatures (n_e up to $\sim$ few 1000 cm^{-3}'; $T_e \gtrsim 14\,000$ K) in the broader, blueshifted components, both of which are expected for shocked gas, due to the large measurement uncertainties, we cannot say with certainty that the densities and temperatures in the broader components are significantly different from those in the narrower components.

In Section 4.2 and Figs 3 and 4, we plotted a variety of diagnostic diagrams, including the latest shock ionization models from Allen et al. (2008) along with some of the older AGN photoionization models (from MAPPINGS and the mixed-medium ($A_{M/I}$) sequence from Binette et al. 1996). However, as discussed above, the evidence from the diagnostic diagrams is far from clear, with only a weak trend for the broader components to be more consistent with fast ($v_{shock} \geq 500$ km s^{-1}) shock plus precursor models.

Our results are, therefore, rather surprising. The evidence in the literature for jet–cloud interactions in the nuclear regions of compact radio sources, based on the emission-line alignments and extreme emission-line kinematics, is strong. However, at best, we have found only weak suggestions of jet–cloud interactions in the optical emission-line ratios. Typically, we have found the emission-line ratios in compact radio sources to be remarkably similar to those in extended sources, with only a mild tendency for the optical line luminosities to be lower in compact radio sources for a given radio power (see Section 4.4). Possible explanations for these apparent contradictions include the following.

(i) *Difficulty in distinguishing between the models.* As already noted in section 4.2 above, it can be difficult to distinguish in the diagnostic diagrams between the results of simple slab AGN photoionization models and the shock + precursor models, and between the mixed medium photoionization models and the shock + precursor models, for some regions of parameter space.

(ii) *AGN photionization masking shock signatures.* It is entirely possible that the emission-line clouds have been accelerated in jet-induced shocks, have cooled behind the shock, and then have been photoionized by the powerful AGN continuum; the AGN may also photoionize the precursor gas. In this way, the AGN may mask the ionizing effects of the jet-induced shocks.

It will be necessary to obtain higher quality, spatially resolved emission-line data (including temperature and density diagnostics) for sources with well-characterized AGN, in order to truly distinguish the dominant ionization mechanism for the warm gas in the compact radio sources.

4.4 How do compact radio sources compare to more extended radio sources?

In addition to the data for this sample (see above), the diagnostic diagrams in Figs 3 and 4 also show data for extended radio sources, including nuclear regions and EELRs, both with and without evidence for jet–cloud interactions (see Fig. 3 for details).

As discussed in Section 4.2, the compact and extended radio sources occupy remarkably similar regions on the diagnostic diagrams. This is a surprising result given the markedly different line profiles and more extreme kinematics observed in the nuclear regions of compact radio sources compared to extended radio sources. There may be evidence in some of the diagrams (e.g. Fig. 4b and c versus Figs 3b and c) of a tendency for the broader, shifted components to be more consistent with the region occupied by the EELRs with evidence for jet–cloud interactions. However, our current sample of compact radio sources is too small to make any concrete statements.

In order to compare the compact and extended radio sources further, we have also plotted radio-optical correlation plots in Fig. 5, following, for example, Morganti et al. (1997) and Tadhunter et al. (1998). Fig. 5 includes all objects from this sample, along with a redshift limited subset ($0.05 < z < 0.7$) of the 2 Jy sample (e.g. Tadhunter et al. 1998).

In Fig. 5, the compact radio sources follow the same trends as the extended sources and occupy the high radio luminosity end of the correlations. Morganti et al. (1997) reported for their small sample (seven sources) that compact radio sources tended to have a lower [O III]λ5007 luminosity at a given radio luminosity. This trend is also seen in our sample (Fig. 5), with the exception of two

[2] Due to the small spatial scales, it is currently not possible to resolve the outflowing regions sufficiently.

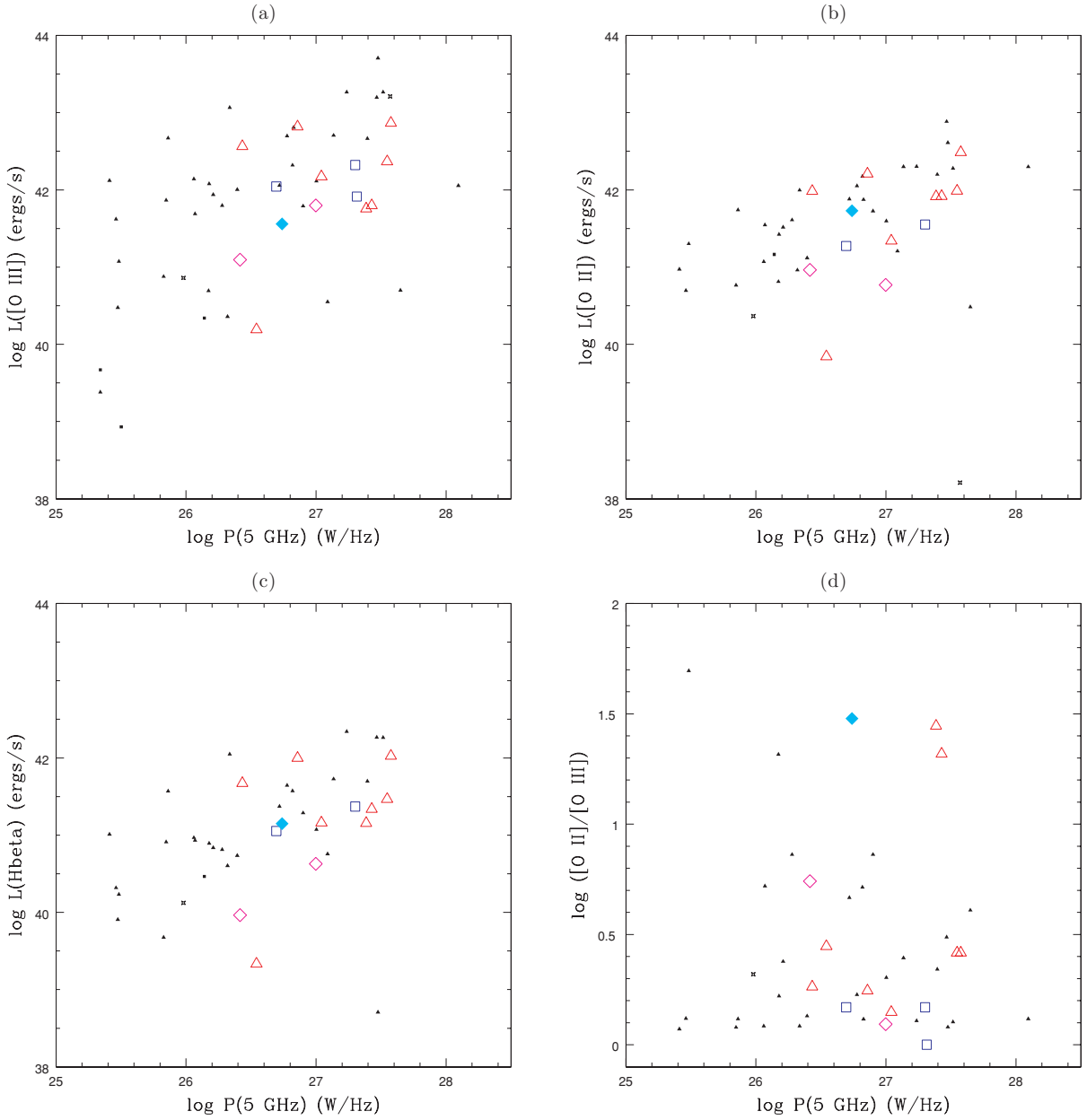

Figure 5. Radio-optical correlation plots. Plotted are the sources from this sample: CSS (red triangles), GPS (blue squares), compact flat spectrum (magenta diamonds) and compact core (cyan diamond). The comparison sample is a redshift selected subsample ($0.05 < z < 0.7$) of the 2 Jy sample (e.g. Morganti, Killeen & Tadhunter 1993; Tadhunter et al. 1993) and is plotted as small filled triangles (FR II sources), small filled squares (FR I sources) and crosses (core-jet sources). The plots are as follows: (a) [O III]5007 luminosity versus 5GHz radio power; (b) [O II]$\lambda\lambda$3727 luminosity versus 5GHz radio power; (c) Hβ luminosity versus 5GHz radio power; (d) [O II]/[O III] ratio versus 5GHz radio power; and (e) [O III]/Hβ ratio versus 5GHz radio power.

sources (3C 277.1 and 3C 303.1) that lie towards the top boundary of the FR II trend. In addition, there is also evidence of this trend in the other lines plotted ([O II]$\lambda\lambda$3727 and Hβ). It is interesting that the compact radio sources tend to fall below the trend for extended sources, particularly as we would expect to observe boosting in the optical flux if ionization mechanisms other than AGN photoionization (e.g. jet–cloud interactions) were important. However, as discussed in Sections 3.3 and 4.1, the nuclear regions of compact radio sources are highly extinguished[3] and this may lead to the mild tendency of compact radio sources to lie below the trend observed for extended radio sources.

Fig. 5 also compares different emission-line ratios with the radio luminosity. Although there appear to be no clear-cut differences between the compact and extended sources in terms of their line ratios, we note that the three GPS sources are amongst the group with the lowest [O II]/[O III] ratios.

5 SUMMARY AND CONCLUSIONS

It is clear that there are several trends regarding the physical conditions and ionization mechanisms observed in compact radio sources. The main conclusions are listed below.

[3] Due to uncertainties in the reddening estimates (see Section 3.3), the line fluxes used in this analysis are not corrected for reddening.

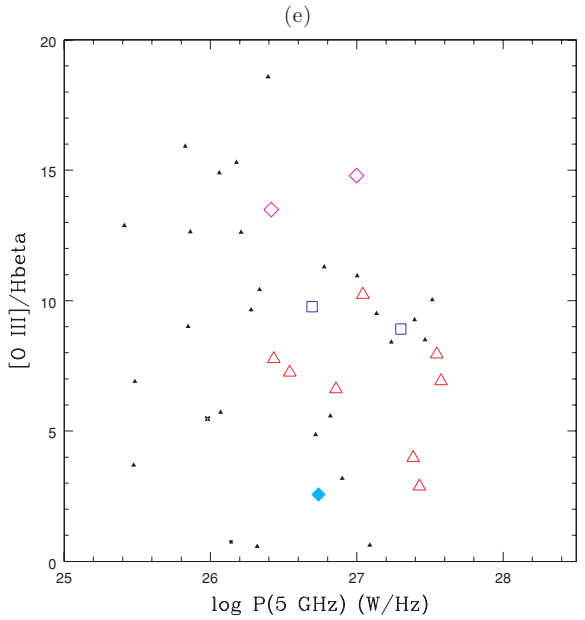

Figure 5 – *continued*

(i) *Dense and dusty circumnuclear cocoons*. The majority of the sources in this sample show evidence for high densities and large reddening in the nuclear regions, particularly in the broader components. 7/14 sources show convincing evidence for increasing reddening with the line width of emission-line component (for the remaining seven sources, four do not show the trend and we were unable to estimate the reddening for three sources), a strong indication of a stratified ISM, as in PKS 1345+12 (see H03). This is also supported by an apparent trend in density with FWHM, although the uncertainties are larger. Hence, the results presented here are entirely consistent with the idea of a dense and dusty cocoon of gas and dust enshrouding the nuclear regions, although evidence suggests that there is insufficient material to confine and frustrate the radio source.

(ii) *Outflow driving mechanisms*. The evidence for jet-driven outflows in the literature is strong. Extreme line broadening and outflow velocities are observed (up to $\sim$2000 km s^{-1}) and there is strong alignment between the radio and optical line emission in *all* CSS sources with *HST* imaging. It is, therefore, surprising that our study has not provided the expected supporting evidence from the emission-line ratios. Whilst our results suggest the gas densities and temperatures may be high, and hint at possible shock ionization in the broader, shifted components, the data do not clearly distinguish between shocks and AGN photoionization.

(iii) *Quiescent, photoionized gas*. As well as the kinematically disturbed gas, we also observe quiescent gas on a variety of scales. In the nuclear regions, the narrow components of the emission-line gas are predominantly AGN photoionized (mainly mixed-medium models), consistent with observations of the nuclear regions of extended sources. In more extended regions, we see evidence for both AGN photoionization and also localized regions of star formation.

(iv) *Similarities with extended sources*. We present evidence for similarities between compact and extended sources suggesting that they are instrinsically similar objects. The high reddening in the nuclear regions is consistent with observations of, for example, Cygnus A (e.g. Taylor et al. 2003). Also, the radio-optical correlations show that compact radio sources agree with the high radio power end of the correlations for extended sources, although there is a mild tendency for the compact radio sources to have lower optical emission-line luminosities ([O II], [O III] and Hβ) for a given radio luminosity. The scatter may be due to the high extinction in the nuclear regions of these sources.

Hence, the evidence presented in this paper is fully consistent with the idea that compact radio sources form the early evolutionary stage in AGN with radio activity.

ACKNOWLEDGMENTS

JH acknowledges financial support from PPARC and NWO. We would like to thank Dr. Brent Groves for making his new Diagnostic Diagram Tool available to us. We also thank the referee for useful comments that have helped to improve the manuscript. The William Herschel Telescope is operated on the island of La Palma by the Isaac Newton Group in the Spanish Observatorio del Roque de los Muchachos of the Instituto de Astrofisica de Canarias. This research has made use of the NASA/IPAC Extragalactic Data base (NED) which is operated by the Jet Propulsion Laboratory, California Institute of Technology, under contract with the National Aeronautics and Space Administration. Based on observations made with ESO Telescopes at the La Silla and Paranal Observatory under programmes 69.B-0548(A) and 71.B-0616(A).

REFERENCES

Allen M. G., Groves B. A., Dopita M. A., Sutherland R. S., Kewley L. J., 2008, ApJS, 178, 20
Axon D. J., Capetti A., Fanti R., Morganti R., Robinson A., Spencer R., 2000, AJ, 120, 2284
Baker J. C., Hunstead R. W., 1995, ApJ, 452, L95
Batcheldor D., Tadhunter C. N., Holt J., Morganti R., O'Dea C. P., Axon D. J., Koekemoer A., 2007, ApJ, 661, L13
Bellamy M. J., Tadhunter C. N., Morganti R., Wills K. A., Holt J., Taylor M. D., Watson C. A., 2003, MNRAS, 344, L80
Best P. N., Kaiser C. R., Keckman T. M., Kauffmann G., 2006, MNRAS, 368, 67
Bicknell G., Dopita M. A., O'Dea C. P., 1997, ApJ, 485, 112
Bicknell G. V., Saxton C. J., Sutherland R. S., Midgley S., Wagner S. J., 2003, New Astron. Rev., 47, 537
Binette L., Wilson A. S., Storchi-Bergmann R., 1996, A&A, 312, 365
Bower R. G., Benson A. J., Malbon R., Helly J. C., Frenk C. S., Baugh C. M., Cole S., Lacey C. G., 2006, MNRAS, 370, 645
Clark N. E., Axon D. J., Tadhunter C. N., Robinson A., O'Brien P., 1998, ApJ, 494, 546
Cohen R. D., Osterbrock D. E., 1981, ApJ, 243, 81
Costero R., Osterbrock D. E., 1977, ApJ, 211, 675
Croton D. J. et al., 2006, MNRAS, 365, 11
de Robertis M. M., Dufour R., Hunt R., 1987, J. R. Astron. Soc. Can., 81, 195
de Vries W. H. et al., 1997, ApJS, 110, 191
de Vries W. H., O'Dea C. P., Baum S. A., Barthel P. D., 1999, ApJ, 526, 27
de Vries W. H., O'Dea C. P., Perlman E., Baum S. A., Lehnert M. D., Stocke J., Rector T., Elstlon R., 1998, ApJ, 503, 138
Di Matteo T., Springel V., Hernquist T., 2005, Nat, 433, 604
Dickson R. D., 1997, PhD thesis, University of Sheffield
Dickson R. D., Tadhunter C. N., Shaw M., Clark N., Morganti R., 1995, MNRAS, 273, 29
Ferrarese L., Merritt D., 2000, ApJ, 539, 9
Ferruit P., Binette L., Sutherland R., Pecontal E., 1997, A&A, 322, 73
Gebhardt K. et al., 2000, ApJ, 539, 13
Grandi S. A., Osterbrock D. E., 1978, ApJ, 220, 783
Guainazzi M., Siemiginowska A., Standhellini C., Grandi P., Piconelli E., Azubike Ugwoke C., 2006, A&A, 446, 87

Holt J., 2005, PhD thesis, University of Sheffield
Holt J., Tadhunter C. N., Morganti R., 2003, MNRAS, 342, 227 (H03)
Holt J., Tadhunter C. N., Morganti R., Bellamy M. J., González Delgado R. M., Tzioumis A., Inskip K. J., 2006, MNRAS, 370, 1633 (H06)
Holt J., Tadhunter C. N., González Delgado R. M., Inskip K. J., Rodriguez Zaurin J., Emonts B. H. C., Morganti R., Wills K. A., 2007, MNRAS, 381, 611
Holt J., Tadhunter C. N., Morganti R., 2008, MNRAS, 387, 639 (H08)
Hopkins P. F., Hernquist L., Cox T. J., Di Matteo T., Martini P., Robertson B., Springel V., 2005, ApJ, 630, 705
Kauffmann G. et al., 2003, MNRAS, 346, 1055
Kewley L., Dopita M., Sutherland R., Heisler C., Trevena J., 2001, ApJ, 556, 121
Marconi A., Hunt L. K., 2003, ApJ, 589, L21
Morganti R., Robinson A., Fosbury R. A. E., di Serego Alighieri S., Tadhunter C. N., Malin D. F., 1991, MNRAS, 249, 91
Morganti R., Killeen N., Tadhunter C. N., 1993, MNRAS, 263, 1023
Morganti R., Tadhunter C. N., Dickson R., Shaw M., 1997, A&A, 326, 130
Morganti R., Tadhunter C. N., Oosterloo T. A., Holt J., Tzioumis A., Wills K., 2003, PASA, 20, 129
Morganti R., Oosterloo T. A., Tadhunter C. N., Vermeulen R., Pihlström Y. M., van Moorsel G., Wills K. A., 2004, A&A, 424, 119
Morganti R., Tadhunter C. N., Oosterloo T. A., 2005, A&A, 444, L9
Privon G. C., O'Dea C. P., Baum S. A., Axon D. J., Kharb P., Buchanan C. L., Sparks W., Chiaberge M., 2008, ApJS, 175, 423
Robinson T. G., 2001, PhD thesis, University of Sheffield
Robinson A., Binette L., Fosbury R. A. E., Tadhunter C. N., 1987, MNRAS, 227, 97
Robinson T. G., Tadhunter C. N., Axon D. J., Robinson A., 2000, MNRAS, 317, 922
Rodriguez Zaurin J., Holt J., Tadhunter C. N., Gonzalez Delgado R. M., 2007, MNRAS, 375, 1133
Schlegel D. J., Finkbeiner D. P., Davis M., 1998, ApJ, 500, 525
Seaton M. J., 1979, MNRAS, 187, 73P
Solorzano-Iñarrea C., 2001, PhD thesis, University of Leeds
Solórzano-Iñarrea C., Tadhunter C. N., 2003, MNRAS, 340, 705
Solórzano-Iñarrea C., Tadhunter C. N., Axon D. J., 2001, MNRAS, 323, 965
Storchi-Bergmann T., Wilson A. S., Mulchaey J. S., Bineette L., 1996, A&A, 312, 357
Tadhunter C. N., 1987, PhD thesis, University of Sussex
Tadhunter C. N., Fosbury R. A. E., Quinn P. J., 1989, MNRAS, 24, 225
Tadhunter C. N., Robinson A., Morganti R., 1989, in Meurs E. J. A., Fosbury R. A. E., eds, ESO Conf. and Workshop Proc. No. 32, ESO Workshop on Extranuclear Activity in Galaxies. ESO, Garching, p. 293
Tadhunter C. N., Morganti R., di Serego Alighieri S., Fosbury R. A. E., Danziger I. J., 1993, MNRAS, 263, 999
Tadhunter C. N., Metz S., Robinson A., 1994a, MNRAS, 268, 989
Tadhunter C. N., Shaw M. A., Morganti R., 1994b, MNRAS, 271, 807
Tadhunter C. N., Morganti R., Robinson A., Dickson R., Villar-Martín M., Fosbury R. A. E., 1998, MNRAS, 298, 1035
Tadhunter C. N., Wills K., Morganti R., Oosterloo T., Dickson R., 2001, MNRAS, 327, 227
Tadhunter C. N., Robinson T. G., González Delgado R. M., Wills K., Morganti R., 2005, MNRAS, 356, 480
Taylor M. D., Tadhunter C. N., Robinson T. G., 2003, MNRAS, 342, 995
Tremaine S. et al., 2002, ApJ, 574, 740
Villar-Martín M., Tadhunter C. N., Morganti R., Clark N., Kileer N., Axon D., 1998, A&A, 332, 479
Villar-Martín M., Tadhunter C. N., Morganti R., Holt J., 2005, MNRAS, 359, L5
Vink J., Snellen I. A. G., Mack K.-H., Schilizzi R., 2006, MNRAS, 367, 928
Wills K. A., Tadhunter C. N., Robinson T. G., Morganti R., 2002, MNRAS, 333, 221

APPENDIX A: THE EMISSION-LINE FLUXES

Table A1 presents emission-line flux data for the sample. This is an extract from the full table, which is available in the online version of the article – see the Supporting Information.

Table A1. Emission-line flux data for the sample.

		3C 213.1 (nuc)	3C 268.3 (nuc)	3C 268.3 (SE)	3C 268.3 (NW)	3C 277.1 (nuc)	3C 277.1 (SE)	3C 277.1 (SE HII)	PKS 1345+12 (nuc)	PKS 1345+12 (NW PA160)	PKS 1345+12 (SE PA160)
Mg II 2795.5	n										
	i										
	b										
	vb										
[O III] 3133.70	n					80 ± 10					
	i					–					
	b										
	vb										
He I 3188.67	n					11 ± 3					
	i					–					
	b										
	vb										
[Ne V] 3345.8†	n			16 ± 1	120 ± 40	17 ± 1	30 ± 10 20 ± 20			2 ± 1	
	i					15 ± 3					
	b										
	vb										
[Ne V] 3425.0†	n	<20	<30	50 ± 2	170 ± 40	50 ± 10	80 ± 30 70 ± 40			6 ± 3	<286 <82
	i	60	<20			50 ± 20					
	b										
	vb										
[O II] 3727.64‡	n	850 ± 30	190 ± 10 220 ± 10	110 ± 4	650 ± 40	160 ± 10	350 ± 50 170 ± 90	200 ± 10		205 ± 5	1179 ± 57 102 ± 16
	i	170	90 ± 10			180 ± 10					
	b										
	vb										
[Fe VII] 3759.99	n					13 ± 2					
	i					–					
	b										
	vb										
Hβ 4860.75†	n	0.9 ± 0.1	0.7 ± 0.1 0.9 ± 0.1	0.97 ± 0.03	0.05 ± 0.02	22 ± 3	0.18 ± 0.03 0.13 ± 0.02	0.31 ± 0.02		2.58 ± 0.14	0.14 ± 0.08 0.49 ± 0.07
	i	<0.8	1.6 ± 0.2			8 ± 3					
	b										
	vb					BLR: 100 ± 10					

Note. This is an extract from the full table, which is available in the online version of the article – see the Supporting Information. All line fluxes are quoted relative to Hβ (=100). The data are given for all apertures for each object, for all lines observed. Column 2 identifies the emission-line component (n = narrow; i = intermediate; b = broad; vb = very broad) in accordance with the width definitions given in Section 2. For objects with a detected BLR, the data for this component are also presented and identified by BLR in the table. The Hβ fluxes are quoted in units of 10^{-16} ergs^{-1} cm^{-2} Å^{-1}.
†Upper limits mean wavelength for doublet blend in low density limit.
‡Weighted mean wavelength for doublet blend in low density limit.

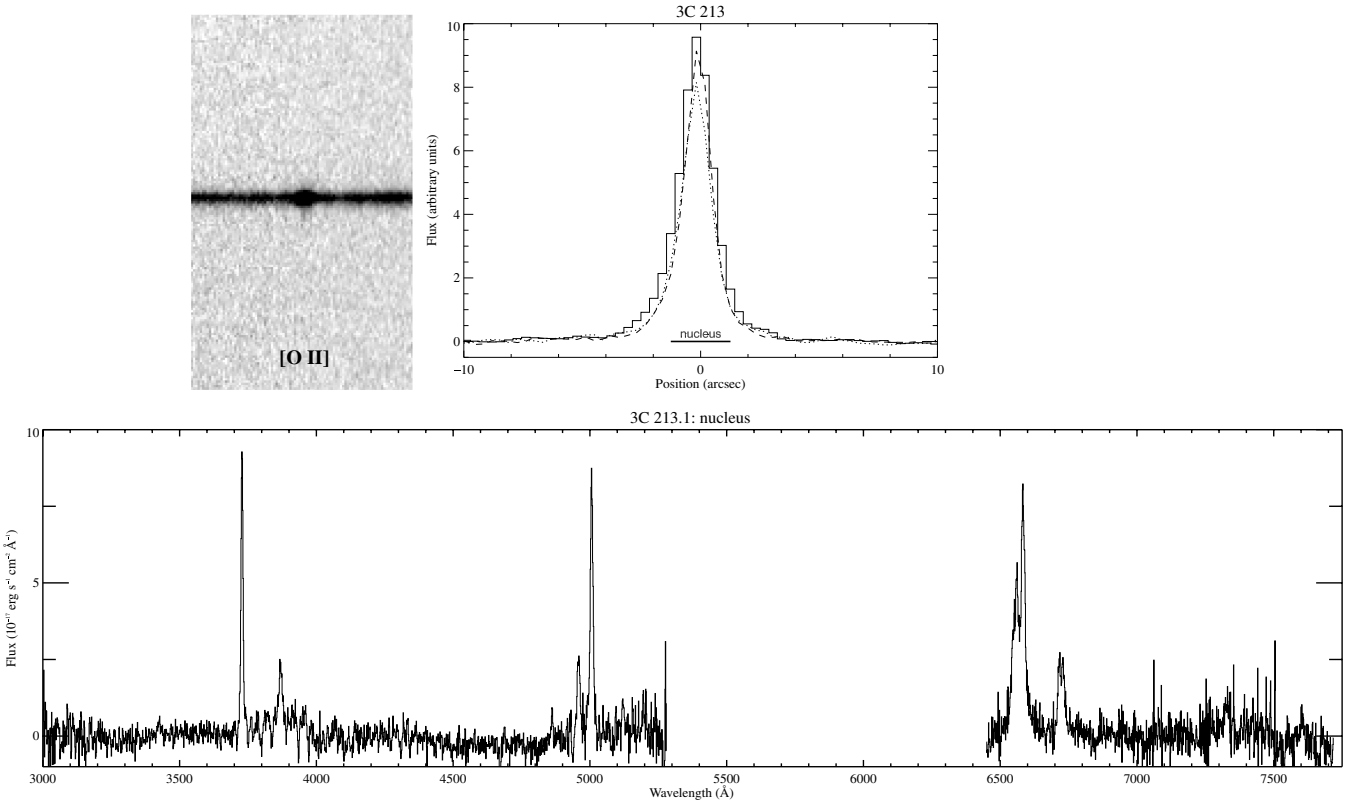

Figure B1. Emission-line spectra for 3C 213.1 along PA -61. Top: spatial profile of the continuum and emission lines in 3C 213.1 along PA-80. The left-hand panel shows the two-dimensional spectrum of the most extended emission line along this PA, [O II]λλ3727 and the right-hand panel shows spatial slices across the spectrum for both [O II]λλ3727 (dotted line) and [O III]λλ4959,5007 (dashed line) emission lines. The fluxes in the different profiles have been scaled for comparison purposes. Overplotted are the positions and sizes of the apertures extracted. Bottom: integrated rest frame, continuum subtracted spectrum of the nuclear aperture.

APPENDIX B: APERTURE SELECTION AND EXTRACTED SPECTRA FOR ALL APERTURES

Fig. B1 shows an extract from the full appendix (containing Figs B1–B12), which is available in the online version of the article – see the Supporting Information.

SUPPORTING INFORMATION

Additional Supporting Information may be found in the online version of this article:

Appendix A. The emission-line fluxes.
Appendix B. Aperture selection and extracted spectra for all apertures.

Please note: Wiley-Blackwell are not responsible for the content or functionality of any supporting materials supplied by the authors. Any queries (other than missing material) should be directed to the corresponding author for the article.

This paper has been typeset from a TEX/LATEX file prepared by the author.